AGU PUBLICATIONS

JGR

Journal of Geophysical Research: Space Physics

RESEARCH ARTICLE
10.1002/2015JA022299

Special Section:
Big Storms of the Van Allen Probes Era

Middle- and low-latitude ionosphere response to 2015 St. Patrick's Day geomagnetic storm

B. Nava[1], J. Rodríguez-Zuluaga[1], K. Alazo-Cuartas[1], A. Kashcheyev[1], Y. Migoya-Orué[1], S.M. Radicella[1], C. Amory-Mazaudier[1,2], and R. Fleury[3]

[1]T/ICT4D, The Abdus Salam International Centre for Theoretical Physics, Trieste, Italy, [2]Sorbonne Paris, UPMC University Paris VI, LPP, Paris, France, [3]Lab-STICC/UMR CNRS, Brest, France

Key Points:
- The 2015 St. Patrick's Day geomagnetic storm has been studied using different kinds of sensors and data
- Prompt penetration and disturbance dynamo electric fields have been analyzed using spectral analysis
- The data analysis results have been interpreted on the basis of theoretical models

Correspondence to:
B. Nava,
bnava@ictp.it

Citation:
Nava, B., J. Rodríguez-Zuluaga, K. Alazo-Cuartas, A. Kashcheyev, Y. Migoya-Orué, S. M. Radicella, C. Amory-Mazaudier, and R. Fleury (2016), Middle- and low-latitude ionosphere response to 2015 St. Patrick's Day geomagnetic storm, *J. Geophys. Res. Space Physics*, *121*, 3421–3438, doi:10.1002/2015JA022299.

Received 22 DEC 2015
Accepted 6 MAR 2016
Accepted article online 10 MAR 2016
Published online 9 APR 2016

©2016. American Geophysical Union. All Rights Reserved.

Abstract This paper presents a study of the St Patrick's Day storm of 2015, with its ionospheric response at middle and low latitudes. The effects of the storm in each longitudinal sector (Asian, African, American, and Pacific) are characterized using global and regional electron content. At the beginning of the storm, one or two ionospheric positive storm effects are observed depending on the longitudinal zones. After the main phase of the storm, a strong decrease in ionization is observed at all longitudes, lasting several days. The American region exhibits the most remarkable increase in vertical total electron content (vTEC), while in the Asian sector, the largest decrease in vTEC is observed. At low latitudes, using spectral analysis, we were able to separate the effects of the prompt penetration of the magnetospheric convection electric field (PPEF) and of the disturbance dynamo electric field (DDEF) on the basis of ground magnetic data. Concerning the PPEF, Earth's magnetic field oscillations occur simultaneously in the Asian, African, and American sectors, during southward magnetization of the B_z component of the interplanetary magnetic field. Concerning the DDEF, diurnal magnetic oscillations in the horizontal component H of the Earth's magnetic field exhibit a behavior that is opposed to the regular one. These diurnal oscillations are recognized to last several days in all longitudinal sectors. The observational data obtained by all sensors used in the present paper can be interpreted on the basis of existing theoretical models.

1. Introduction

This paper is devoted to the study of the St Patrick's Day storm of 2015, currently the largest geomagnetic storm occurred since the beginning of the low solar cycle 24. Since more than several decades, storms are the object of many studies. It is well known that during magnetic storms, energy is transferred from the solar wind to the magnetosphere. The region of strong coupling between the interplanetary medium, the magnetosphere, the thermosphere, and the ionosphere is the auroral region. In this region, storms increase the auroral electric currents mainly through (1) the precipitation of particles which increases the ionospheric conductivities, (2) the field aligned currents closing through perpendicular currents in the ionosphere, and (3) the mapping of the magnetospheric convection electric field. The auroral electric currents transfer energy to the neutral gas via Joule heating, $\mathbf{J}\cdot\mathbf{E}$ ($\mathbf{J}$, electric current density; $\mathbf{E}$, electric field). They move also the neutral wind via momentum transfer by the Ampere force $\mathbf{J}\times\mathbf{B}$ ($\mathbf{B}$, geomagnetic field). Joule heating and momentum force drive thermospheric winds and pressure fields and produce gravity waves and equatorward thermospheric winds at *F* region heights [*Testud and Vasseur*, 1969; *Richmond and Roble*, 1979]. These thermospheric winds extend from the auroral to middle and low latitudes [*Mazaudier and Bernard*, 1985; *Mazaudier et al.*, 1985] with a return flow at *E* region altitudes around the equator: the so-called Hadley cell. These winds also lift the ionization to regions of lower loss, producing daytime increases in h_mF_2, in f_oF_2, including total electron content (TEC) and global changes in the atmospheric composition [*Jones*, 1971; *Jones and Rishbeth*, 1971; *Volland*, 1979].

In the electrodynamics coupling between high and low latitudes there are two main physical processes acting at a planetary scale: (1) the prompt penetration of magnetospheric convection electric field (PPEF) at the origin of the disturbance polar no. 2 (DP2) equivalent current system [*Nishida et al.*, 1966; *Nishida*, 1968] and first modeled by *Vasyliunas* [1970] and (2) the dynamo effects of the storm winds disturbance dynamo electric field (DDEF), first predicted by *Blanc and Richmond* [1980] and isolated using ground magnetic data by *Le-Huy and Amory-Mazaudier* [2005] and called D_{dyn} current system.

In the last decades, the PPEF and its mapping from high to low latitudes has been studied [e.g., *Kikuchi and Araki*, 1979; *Kikuchi et al.*, 1996; *Fejer and Scherliess*, 1997; *Abdu et al.*, 1998; *Peymirat et al.*, 1998; *Kobea et al.*, 2000].

Several works have been carried out about ionospheric perturbations at equatorial latitudes related to disturbances in the ionospheric dynamo [*Fejer et al.*, 1983; *Sastri*, 1988; *Mazaudier and Venkateswaran*, 1990; *Abdu et al.*, 1997].

Previous studies of St Patrick's Day storm were made by *Zhang et al.* [2015] on geomagnetically induced current (GIC), by *Cherniak and Zakharenkova* [2015] on the high-latitude plasma irregularities and by *Tulasi Ram et al.* [2016] on the response of the equatorial zonal electric field to PPEF. Indeed, *Astafyeva et al.* [2015] carried out a global overview of the ionospheric response during this storm using a multi-instrument approach, indicating a hemispheric asymmetry in different longitudinal sectors.

In this work diverse kinds of data and analysis techniques have been simultaneously used to present the ionosphere behavior during the storm at a global scale, with particular focus on middle and low latitudes. Ground-based Global Navigation Satellite Systems (GNSS)-derived TEC data (vertical TEC (vTEC) map, global electron content (GEC), and regional electron content (REC)) have been used to analyze the ionosphere response to PPEF and DDEF. For the first time in relation to this storm, PPEF and DDEF have been studied applying spectral analysis to magnetic field data, as recorded by magnetometers on the ground. Satellite measured [O/N_2] data and ionosonde-derived peak parameter values have been finally considered to complete the storm effects overview also in terms of composition, regional change in electron density, and variation in ionospheric F_2 layer height.

Section 2 is devoted to the description of data sets and data processing and section 3 to the presentation of the results. In section 4 we discuss the results in light of the different physical processes and models and then we summarize this work and conclude in the last section.

2. Data Sets and Data Processing

2.1. Data Sets

Data sets used to characterize the St Patrick's Day storm and its recovery phase include data from the Sun to the Earth.

Regarding the Sun, the SOHO satellite data give the type of solar disturbance, (coronal mass ejection (CME), high-speed solar wind stream (HSSWS)) that are at the origin of the ionospheric disturbance, www.nasa.gov/mission_pages/soho/.

With reference to the solar wind, the ACE satellite provides the B_z component of the interplanetary magnetic filed (IMF) and the solar wind speed (V_{sw}) which are key parameters for storm studies, http://omniweb.gsfc.nasa.gov/.

In the magnetosphere, the sudden storm commencement (SSC) indicates the beginning of the storm and the magnetic index *SYM-H* characterizes the magnetospheric electric currents. In the auroral ionosphere, the *AE* magnetic index is an indicator of the energy transmitted to the Earth's environment during the storm. The *SYM-H* and *AE* magnetic indices are provided by the World Data Center for Geomagnetism, Kyoto http://wdc.kugi.kyoto-u.ac.jp.

In the ionosphere, we computed TEC data for more than 100 single GNSS receivers to perform a local analysis of TEC variations and we used vTEC data from global ionospheric maps (GIM) in order to establish a global overview of the ionosphere behavior during the period under analysis.

The GNSS data have been extracted from the following websites: the EUREF Permanent Network: http://www.epncb.oma.be/, the Scripps Orbit and Permanent Array Center: http://sopac.ucsd.edu/, the UNAVCO consortium: http://www.unavco.org/, and the International GNSS Service (IGS): http://igs.org/. We analyzed also the Earth's magnetic field variations recorded by three magnetometers located at low latitudes and belonging to INTERMAGNET (http://intermagnet.org) and to the Low-Latitude Ionospheric Sensor Network (http://lisn.igp.gpb.pe). Ionospheric data were obtained from three ionosondes (http://umlcar.uml.edu/DIDBase/). Manually scaled peak parameter data have been considered for the F_2 ionospheric layer analysis, [*Reinisch and Galkin*, 2011].

Figure 1 shows the location of the magnetic observatories, ionosondes, and some representative GNSS stations located at middle and low latitudes. Modip [*Rawer*, 1963] isolines (green) are also indicated. Table 1

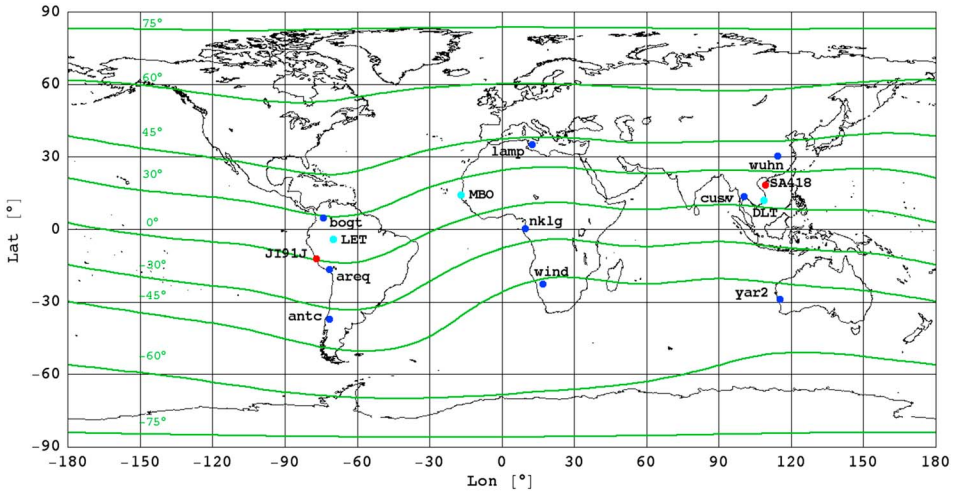

Figure 1. Location of the magnetometers (light blue), ionosondes (red), and some representative GNSS stations (blue) used in the present work. Modip isolines (green) are also indicated.

gives the geographic coordinates of these sensor stations. It has to be considered that the location of these observatories also determined the definition of the longitudinal sectors used in the present paper.

2.2. Data Processing

2.2.1. GPS Data

The slant total electron content (sTEC) values for single receivers were retrieved from the Global Positioning System (GPS) measurements. Since the TEC is not a direct measurement, a "debiasing" procedure or calibration [*Ciraolo et al.*, 2007] has been applied to obtain the sTEC values from the raw GPS observables.

Then, the vTEC over a given receiver has been computed using a least square estimation applied to the same set of coefficients retrieved with the procedure mentioned above.

2.2.2. vTEC Maps

As far as global maps are concerned, the relevant vTEC data have been obtained from the Universitat Politecnica de Catalunya (UPC) global ionospheric maps (GIM) (named "UQRG"). These vTEC maps are computed from GPS data using ionospheric tomographic and kriging techniques [*Hernandez-Pajares et al.*, 1999; *Orus et al.*, 2005], respectively; one recent application and assessment can be found in *Gulyaeva et al.* [2013].

Table 1. Geographic Coordinates of the Magnetometers, GPS Stations, and Ionosondes

ID	Geographic Latitude	Geographic Longitude
	GNSS Receivers	
cusv	13.7°N	100.5°E
wuhn	30.5°N	114.3°E
yar2	29.0°S	115.3°E
lamp	35.3°N	12.6°E
nklg	0.3°N	09.7°E
wind	22.6°S	17.1°E
areq	16.5°S	71.5°W
bogt	4.7°N	74.1°W
antc	37.1°S	71.5°W
	Magnetometers	
dlt	11.9°N	108.5°E
mbo	14.3°N	17.0°W
let	4.2°S	70.0°W
	Ionosondes	
SA418	18.3°N	109.4°E
JI91I	12.1°S	77.0°W

2.2.3. GEC and REC

The global electron content (GEC) is defined as a total number of electrons in the near-Earth space environment (from the ground up to the altitudes of GPS satellites) [*Afraimovich et al.*, 2006]. It is calculated using GIM of TEC by the summation of the TEC values in a cell $I_{i,j}$ by the cell's area $S_{i,j}$ over all GIM cells.

$$\mathrm{GEC} = \sum I_{i,j} \cdot S_{i,j} \qquad (1)$$

In this paper, we have used UPC GIM at 15 min time interval. The regional electron content (REC) is defined as a total number of electrons in the four longitudinal sectors: Asia (60°E:150°E), Africa (−30°E:60°E), America (−120°E:−30°E), and Pacific (−180°E:−120°E; 150°E:180°E) and calculated in a similar way to GEC. 1 GEC unit (GECU) = 10^{32} el.

2.2.4. Magnetometer Data

In order to analyze the ionospheric *E* region response to the geomagnetic storm on 17 March 2015, three magnetometers at three different longitudinal sectors, Asian, African, and American, have been used. Their location is shown in Figure 1, and it is reasonably well suited to describe the behavior of the *E* region at low latitudes. The aim of this choice is to evaluate disturbances in the ionosphere (D_I) produced by electric fields and currents at *E* region heights during the event. The period of interest starts on 14 March and lasts until 31 March 2015. The data have a time resolution of 1 min.

The process to separate D_I from the magnetic data is given by

$$D_I^H = H - H_0 - S_R^H - D_M \tag{2}$$

where D_I^H is the disturbance D_I derived from the horizontal component (H) of the Earth's magnetic field; H_0 is the magnetic field component due to the Earth's external core dynamics, S_R^H is the daily quiet regular variation of H due mainly to the Sq system, and D_M represents the disturbances coming from the magnetosphere. To calculate D_M, we assume that the largest influence on H during daytime is coming from the symmetric ring current. Then we use the *SYM-H* index and the dip latitude ϕ to normalize the effect of the ring current at each station as follows:

$$D_M = SYM\text{-}H \cdot \cos\phi \tag{3}$$

The S_R^H is computed using the four geomagnetically quietest days before the storm with $Kp < 2^+$ and it is derived by means of:

$$S_R^H = \frac{1}{n}\sum_{i=1}^{n}\left(H_i - D_i^H\right) - H_0 \tag{4}$$

where n is the number of the quiet days used, H_i is the H field component, and D_i^H the disturbances due mainly to magnetosphere D_M and ionosphere D_I. In this case, the probable D_I occurred during the geomagnetically quietest days is removed using a fitting.

Once the D_I^H has been computed, a spectrum analysis is performed using a continuous wavelet transform in order to detect the relevant periods associated with the phenomenon. The method implemented is the Morlet wavelet. Afterwards, using a high-pass filter, we extract from D_I^H the periods lower than 4 h that are magnetic oscillations related with DP2 fluctuations [*Nishida*, 1968] during PPEF [*Vasyliunas*, 1970]. The second component isolated from D_I^H using a band-pass filter is the diurnal period, as it is expected to be the most relevant one at dynamo heights. This diurnal component is associated to the ionospheric disturbance dynamo D_{dyn} [*Blanc and Richmond*, 1980; *Le-Huy and Amory-Mazaudier*, 2005] as it will be explained later in the present paper.

3. Results

3.1. Overview of the Case

On the website http://www.spaceweather.com, the description of the solar event and the prediction of its geomagnetic effect were done as follows: "March 15th began with a bang. Between 00:45 UT and 02:00 UT a magnetic filament erupted in concert with a slow C9-class solar flare from sunspot AR2297. The combo blast hurled a CME into space. Modeling by NOAA analysts suggests that the cloud will deliver a glancing blow to Earth's magnetic field during the late hours of March 17th." Finally, the CME hits the Earth on March 17 at 04:45 UT. On the days after the CME the Earth was inside the flow of HSSWS.

The Figure 2 (top) shows various global parameters highlighting the features of the period from 14 March to 31 March 2015. The Figure 2 (bottom) is a zoom on the day of the storm and reports B_z, the magnetic indices *AE* and *SYM-H*, and the GEC. The shock of the CME, as detected by the SSC, is indicated by a vertical line. On 17 March 2015, this shock is associated to an increase in the B_z component of the IMF (+10 nT to +26 nT), an increase in the solar wind speed (400 km/s to 520 km/s) and an increase in the magnetic *SYM-H* index (+10 nT to +60 nT). A small peak of 300 nT is also observed at the same time in the *AE* magnetic index. During 17 March 2015, the B_z component of the IMF turns southward around 06:00 UT and reaches the value of −22 nT around 06:20 UT. The compression phase lasted from 04:45 UT to 06:20 UT. At the end of the

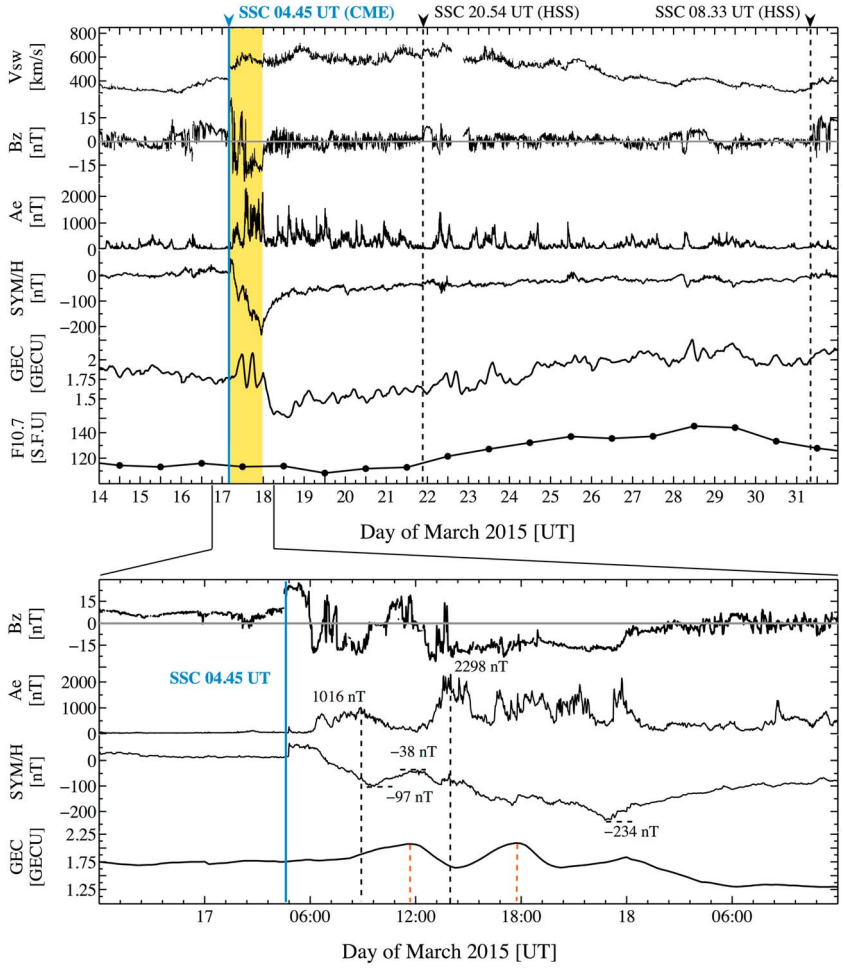

Figure 2. Sun-Earth global parameters, from 14 to 31 March: (from top to bottom) the solar wind speed in km/s, the B_z component of the IMF in nanotesla, the *AE* magnetic index in nanotesla, the *SYM-H* magnetic index in nanotesla, and GEC in GECU and $F_{10.7}$ in solar flux unit.

compression phase, the *AE* magnetic index increases and reaches the maximum value of 1016 nT around 09:30 UT and the *SYM-H* decreases and reaches the minimum value of −97 nT around 10:00 UT. From ~ 09:30 UT until 12:00 UT the B_z is northward. During this period the *AE* index decreases from 1016 nT to ~ 50 nT and the *SYM-H* increases from −97 nT to −38 nT. It is a partial recovery phase. After 12:00 UT the B_z becomes southward again and remains southward until 24:00 UT, except during a very short period around 13:00 UT. During this second period of southward B_z the *AE* index reaches the maximum value of 2298 nT around 13:00 UT and remains large (~1500 nT) until the end of the day. The *SYM-H* slowly decreases from 12:00 UT to 24:00 UT and reaches its minimum value −234 nT before midnight. This is the end of the main phase of the storm that lasted 18 h.

During the period from 18 March 2015 to 31 March (Figure 2, top), the B_z component oscillates. The solar wind speed remains greater than ~ 550 km/s until 26 March 2015. The high values of V_{sw} and the oscillating B_z are the signatures of the high-speed solar wind flowing around the Earth. From 18 March to 25 March 2015, the magnetic index *SYM-H* increases very slowly. It is the recovery phase of the storm which lasts more than 7 days. During the recovery phase, under the effect of HSSWS, the magnetic index *AE* exhibits many peaks larger than 800 nT.

In Figure 2 (top), the two bottom curves are the GEC and the 10.7 cm wavelength solar radio flux ($F_{10.7}$). On 17 March 2015, the GEC exhibits two large increases and a third small one followed by a large decrease starting on 18 March, which lasts more than 1 day. The two large increases of GEC occur several hours after the two increases of *AE* index (see Figure 2, the zoom). From 19 March to 31 March 2015, the GEC slowly increases.

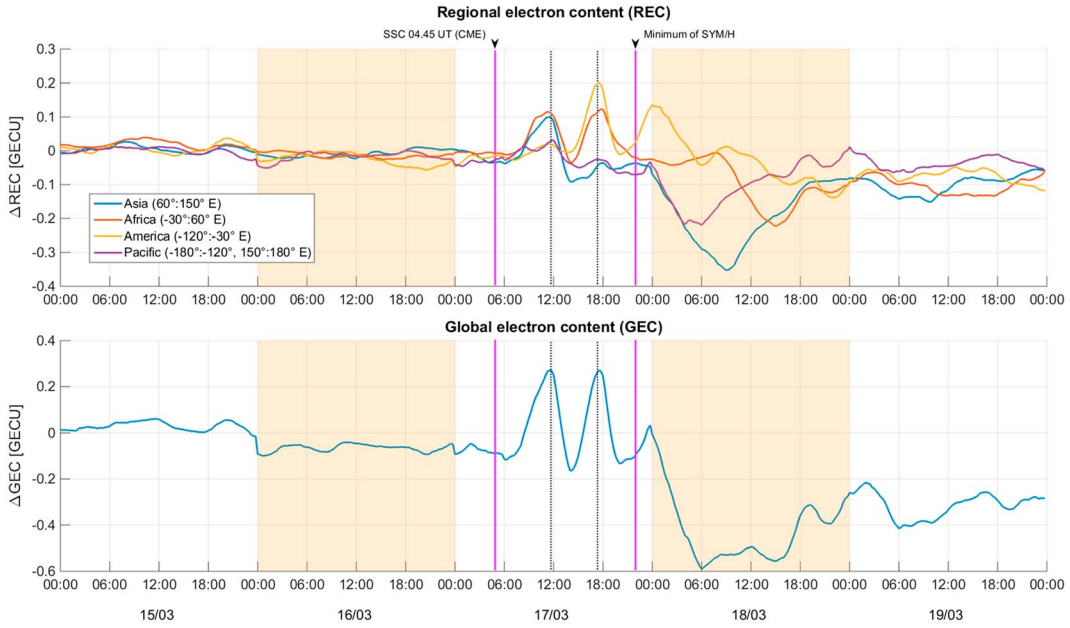

Figure 3. (top) ΔREC, in the four longitudinal sectors Asian, African, American, and Pacific and (bottom) ΔGEC.

$F_{10.7}$ remains at 120 solar flux unit (sfu), from 14 to 21 March 2015, and then it increases slowly. As a consequence, we can deduce that the variation of GEC from 14 to 21 March is not related to the solar flux, which is constant during this period. On the contrary, from 21 to 31 March 2015, the effect of solar flux should be taken into account in the variation of the GEC. In order to explain the peaks observed on GEC we have plotted in Figure 3 (top) ΔREC for the different longitudinal sectors. Each line in this plot shows the difference between the REC of a sector (American, African, Asian, and Pacific) and its average daily values calculated using three quiet days before the storm. In Figure 3 (bottom) ΔGEC is plotted as well.

This figure clearly highlights that the first peak of GEC is mainly related to the Asian and African sectors. The second peak is mainly related to the African and American sectors. The third peak is mainly produced in the American sector. This Figure 3 shows also that the decrease occurs first in the Asian and Pacific sectors, then in the African sector and later in the American one. The largest decrease is clearly in the Asian sector. The decrease is reduced from Pacific to Africa and then to America. In Table 2, columns 2 and 3 give the time and the amplitude of ΔREC.

Table 2. Main Characteristics of the Effect of the Storm in Each Longitudinal Sector; Column 2: Positive Storm, Column 3: Negative Storms, Column 4: Duration of the vTEC Decrease at Middle and Low Latitudes, Column 5: Signature of PPEF, Column 6: Duration of the Diurnal DDEF, Column 7: Periods of the Planetary Waves

Sectors	REC Positive (Figure 3)	REC Negative (Figure 3)	vTEC map Return to Normal (Figure 4)	PPEF (Figures 8 and 9)	DDEF Duration (Diurnal) (Figure 8)	Planetary Waves
Asian	17 March 11:30 UT; ΔREC = 0.099	17 March 14:15 UT; ΔREC = −0.092 18 March 09:00 UT; ΔREC = −0.353	25 March 8 days	Yes during southward B_z	Yes 8 days	5 days 9 days
African	17 March 11:15 UT; ΔREC = 0.116 17:45 UT; ΔREC = 0.123	18 March 07:45 UT; ΔREC = −0.006 15:00 UT; ΔREC = −0.223 21:30 UT; ΔREC = −0.124	23 March 6 days	Yes during southward B_z	Yes 6 days	10.5 days
American	17 March 17:30 UT; ΔREC = 0.201 18 March 00:00 UT; ΔREC = 0.136	18 March 08:45 UT; ΔREC = 0.012 22:00 UT; ΔREC = −0.138	23 March 6 days	Yes during southward B_z	Yes 5 days	5.5 days 9.5 days
Pacific		17 March 23:45 UT; ΔREC = −0.032 18 March 06:00 UT; ΔREC = −0.220				

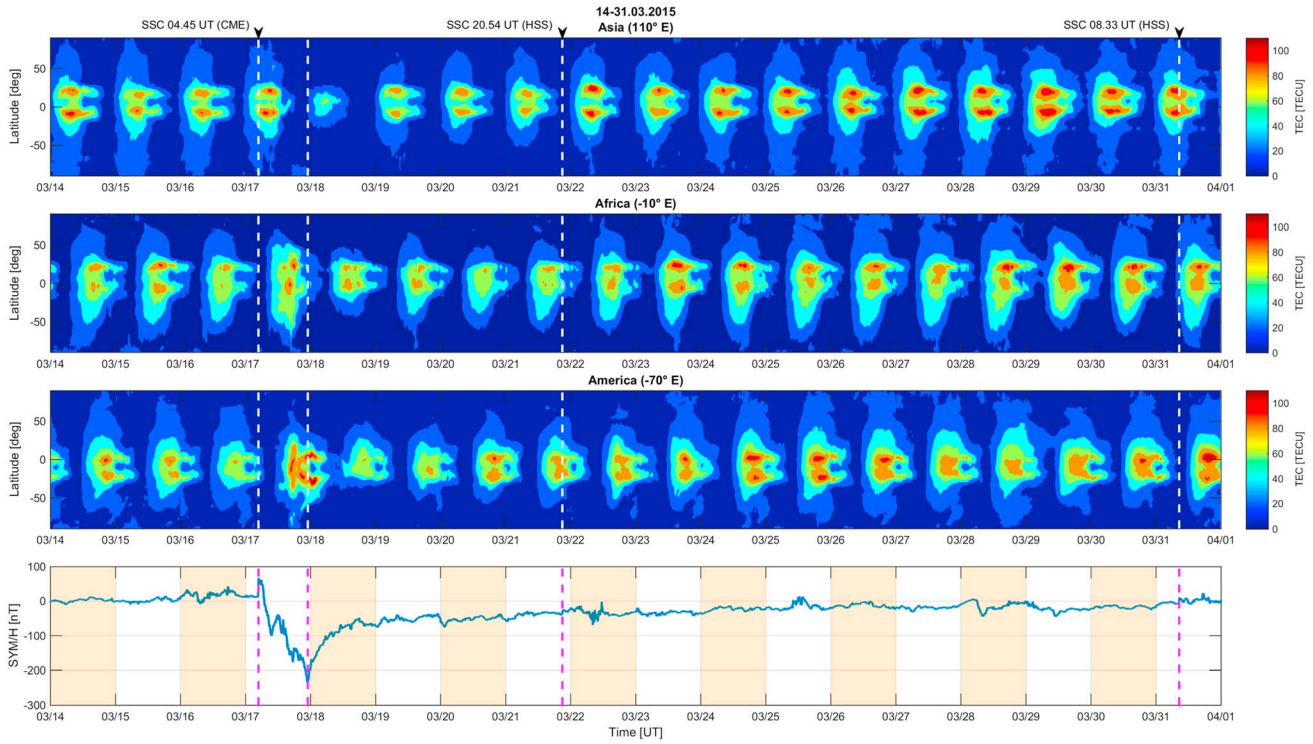

Figure 4. vTEC from 14 to 31 March at specific longitudes representing: the (first panel) Asian sector, (second panel) the African sector, and (third panel) the American sector.

Figure 4 is composed of four panels; the first to third panels show the vTEC as a function of time and latitude at longitudes 110°E, −10°E, and −70°E representing the Asian, African, and American sectors respectively. The vTEC maps cover the period from 14 March to 31 March 2015. In Figure 4 (fourth panel) there is the magnetic index *SYM-H*. Four vertical lines are drawn, the first one indicates the SSC when the CME hits the Earth, the second one indicates the end of the main phase of the storm, and the third and fourth ones indicate other SSC related to HSSWS. A common feature found in all the longitudinal sectors and displayed in Figure 4 is an increase of TEC at the beginning of the storm (particularly evident at the crests of the equatorial anomaly), followed by a TEC decrease (particularly strong at middle and high latitudes if compared to equatorial latitudes). However, substantial differences are observed in the different longitudinal sectors:

1. In the American sector there is a very large increase of vTEC with a very complex structure and a clear latitudinal separation of the crests of the anomaly.
2. In the Asian sector there is a very strong decrease of vTEC starting on late 17 March and continuing on 18 March, when most of the electron content is confined in the equatorial zone.
3. In the American sector, the ionization (vTEC) almost disappears on the south side of the geomagnetic equator, from 18 March until 20 March.
4. In the Asian sector, the vTEC behavior is mostly regular. Every day we observe well-defined crests of vTEC, except on 18 March, the day after the storm.
5. In the African and American sector, the vTEC pattern is irregular. During the storm we observe sometimes two crests and sometimes one crest of ionization.
6. At middle and high latitudes, the return to the normal pattern, i.e., same level of ionization as it was before the storm, occurs on 25 March in the Asian sector and on 23 March in the African and American sectors. In column 4 of Table 2 the duration of the disturbance in each longitudinal sector has been reported.

It is important to notice that in the three longitudinal sectors, on 22 March, the amplitude of the vTEC at the crests is higher than on the days before the storm; this could be due to the HSSWS effect.

Figure 5 shows maps of the [O/N_2] from the Global Ultraviolet Imager (GUVI) for 4 days: 16 March 2015, the day before the storm (bottom left), 17 March 2015, the day of the storm (bottom right) and the 2 days after the

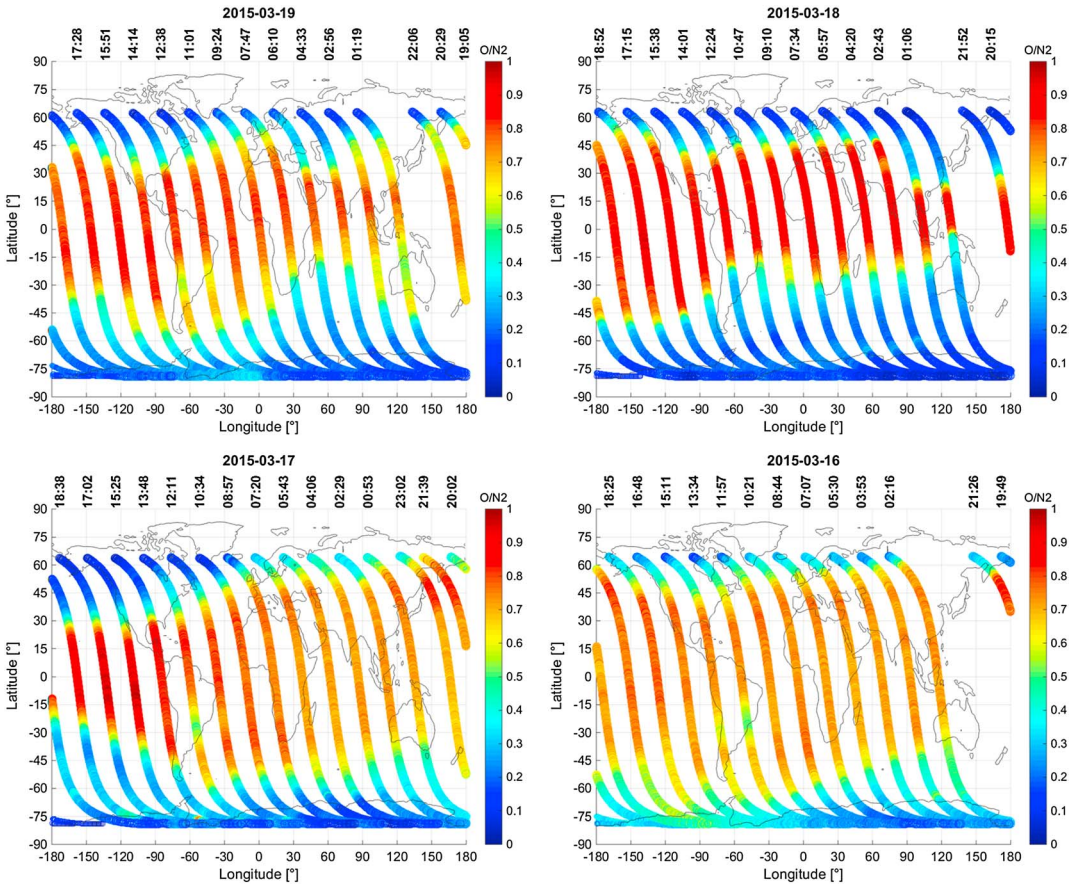

Figure 5. Maps of [O/N_2] from GUVI for 4 days: (top left) 16 March 2015, (top right) 17 March 2015, (bottom left) 18 March 2015, and (bottom right) 19 March 2015.

storm: 18 March 2015 (top right) and 19 March 2015 (top left). The plots show the column O/N_2 ratio derived from the GUVI on board of the NASA Thermosphere Ionosphere Mesosphere Energy and Dynamics satellite. Each plot represents 24 h of the day at nearly constant local time (10:00 LT) as the Earth rotates under the satellite orbit. Time ticks on the top of each plot correspond to the most northern points of the satellite orbits.

We observed a different pattern of [O/N_2] on 17–18 March. In particular, on 18 March there is a large decrease of [O/N_2] in the Asian sector and in the southern part of the American sector. These observations are in good agreement with what is observed in Figure 4.

3.2. Middle- and Low-Latitude Signatures at Specific Locations

In the previous paragraph we analyzed the global pattern of the TEC during the storm period; in this paragraph we will present the observations of the same parameters at specific locations in order to have more detailed analysis of the data at regional scale.

Figure 6 presents the variation of the vTEC for individual stations of the Asian, African, and American sectors, from 14 to 31 March 2015. On each panel the vTEC (in blue), its average daily value (in red) and its standard deviation range (in gray) are shown. The average daily value has been computed using the data from 11 to 16 March (a geomagnetically undisturbed period). For all these days *Ap* is below 22 nT. Figure 6 (first to third panels) is for the Asian sector. At the two middle-latitude stations, wuhn (Northern Hemisphere) and yar2 (Southern Hemisphere), we observe the large decrease of the vTEC during several days after the storm. At the low-latitude station (Northern Hemisphere), cusv, we observe an increase of vTEC on the day of the storm and no decrease on the days after. These observations correspond well to the maps of the Asian sector (Figure 4), and indeed, the maps indicate that on the days after the storm the ionization is confined at low latitudes near the equator, and it almost disappears at middle latitudes.

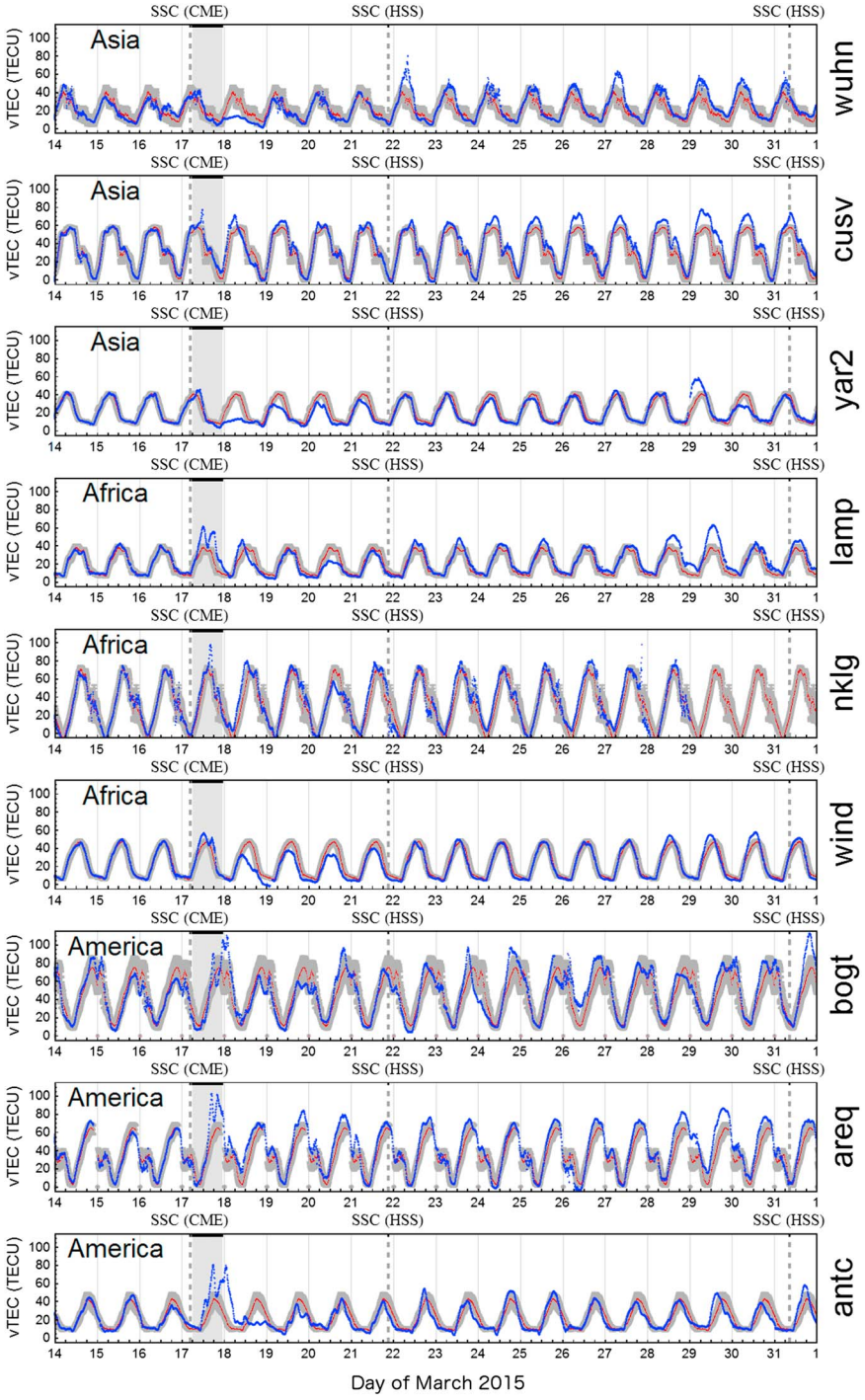

Figure 6. vTEC from 14 to 31 March in the Asian, African, and American sectors. On each panel the vTEC (in blue), its mean quiet value (in red), and its standard deviation range (in gray) are superimposed.

Figure 6 (fourth to sixth panels) corresponds to the African sector. On the day of the storm we observe an increase of vTEC in the three stations lamp (northern low latitude), nklg (equatorial latitude), and wind (southern low latitude) with a double peak structure at middle latitudes (lamp and wind). During the days after the storm from 18 to 20 March the two stations at middle latitudes (lamp and wind) show a vTEC decrease.

Figure 6 (seventh to ninth panels) corresponds to three GNSS stations of the American sector, bogt (equatorial latitude), areq (equatorial trough), and antc (southern middle latitude). On 17 March, the day of the storm the

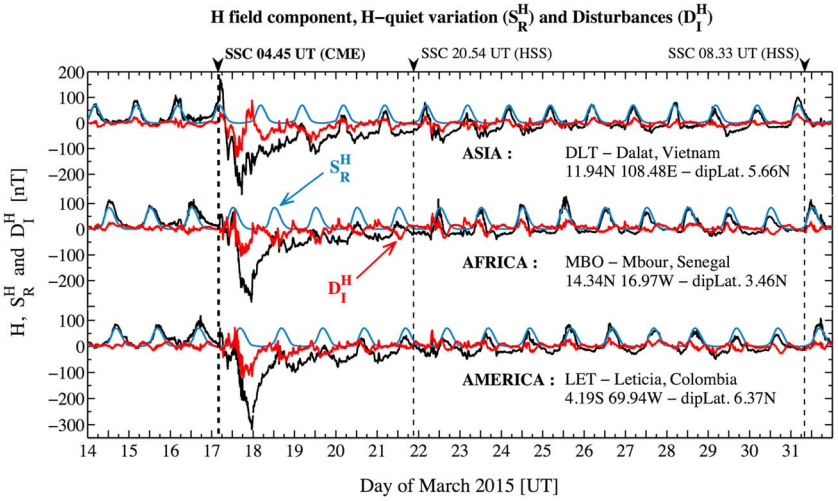

Figure 7. Magnetometer *H* variations at specific longitudinal sectors, from 14 to 31 March: (top) Dalat/Vietnam (Asian sector), (middle) M'bour/Senegal (African sector), and (bottom) Leticia/Colombia (American sector). On each panel the regular variation of the *H* component (blue), the observed *H* component (black), and the disturbed ionospheric electric currents D_I^H (red) are indicated.

three stations exhibit the same behavior, i.e., a very strong increase of vTEC with a multipeak structure. On the day after the storm, the ionization almost disappears at the southern middle latitude station of antc.

In Figure 7, the horizontal magnetic field component *H* (black), its quiet daily variation S_R^H (blue) (4) and the disturbances D_I^H (red) (3) are presented for the three sectors. As it was highlighted in Figure 2, the three events indicated by the dashed lines, correspond to the impact of a CME on 17 March and the arrival of two HSSWS on 21 and 31 March. As it is expected, common patterns are noticed in the *H* component of the geomagnetic field (black line) during the geomagnetic storm in all sectors at the same UT. The first pattern is the increase at the SSC related to the Chapman-Ferraro current during the compression of the magnetosphere [*Chapman and Ferraro*, 1931]. A second global pattern in *H* is its strong decrease due to the ring current effect that is observed during the main phase of the storm. Small differences are noticed at the three sectors during the first hours of the main phase. They are due to local time effects as daytime electric currents like, e.g., equatorial electrojet as well as electric fields owing PPEF could oppose to the ring current. An evident third pattern during the recovery phase is noticed. After the strongest decrease in *H*, a recovery phase (mainly due to the decreased effects of the ring current) lasting until the end of March is also observed in Figure 7. It is also necessary to point out that the lifetime of the recovery phase is affected by the HSSWS event on late 21 March adding some energy into the magnetosphere. With reference to D_I^H the patterns (red line) presented are equal in behavior but different in their temporal occurrence. During 17 March, a decrease is observed firstly in the Asian sector followed by the African and American sectors. The decrease detected is repeated during several days, but its magnitude gradually declines.

A wavelet transform has been applied to the computed D_I^H (2) and its power spectrum is displayed in Figure 8. The wavelet power spectrum (WPS) is presented from top to bottom for the Asian, African, and American sector, respectively. Four common features are highlighted during the event. The first feature is the evident increase in the power of periods between 12 h and 24 h during 17 March corresponding to the main phase of the storm. A second characteristic is the presence of 24 h period oscillations during some days after 17 March. These oscillations last for almost 8 days at Asian sector, 6 days in the African sector, and about 5 days in the American sector. The duration of the diurnal oscillations for the three longitudinal sectors is reported in column 6 of Table 2. The third feature corresponds to short-term oscillations of about 3 h periods present almost during the whole event starting on 17 March up to 24 March. These periods could be related to DP2 fluctuations during PPEF, and their possible evidence could be found in Figure 9. Another remarkable feature is the presence of planetary waves of approximately 5 and 9 days of periodicity. As it is shown in the three panels, the periodicities differ from one sector to another, especially those recorded in the African sector. This finding indicates a possible increase in the strength of planetary waves during

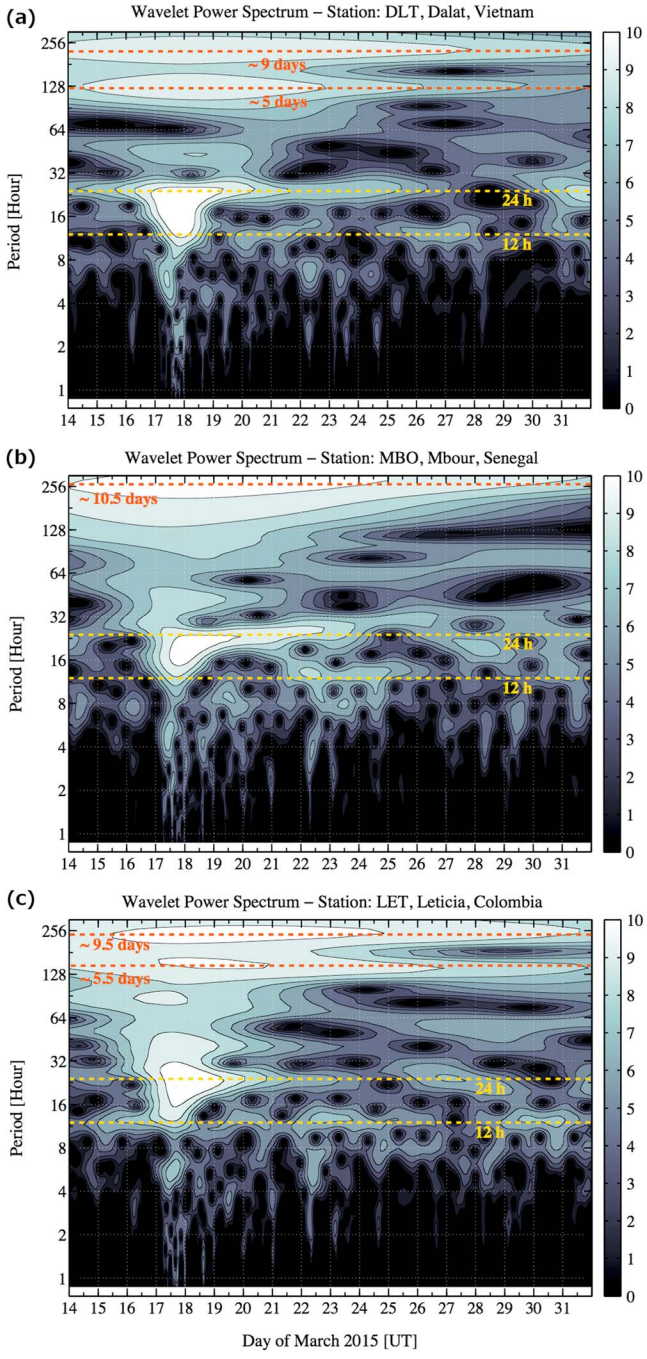

Figure 8. Wavelet power spectrum at specific longitudinal sector, from 14 to 31: (top) Dalat/Vietnam (Asian sector), (middle) M'bour/Senegal (African sector), and (bottom) Leticia/Colombia (American sector).

geomagnetic activity as detected by the wavelet analysis. Indeed, evidence of planetary waves in the lower thermosphere with oscillation periods about 2 to 20 days range has been presented [*Chen*, 1992; *Harris*, 1994; *Forbes et al.*, 1995; *Gurubaran et al.*, 2001; *Takahashi et al.*, 2002; *Pancheva et al.*, 2004]. These planetary fluctuations have been observed to be developed in the troposphere-stratosphere regions and propagating to the mesosphere and lower thermosphere [*Abdu et al.*, 2006]. Nevertheless, the physical mechanism of upward propagation of these oscillations is not yet fully understood [*Forbes*, 1996]. We also included in column 7 of Table 2 the periods of these planetary waves.

Using a high-pass filter, short-term oscillations contained in D_l^H have been isolated and presented in Figure 9. The most important observation is the presence of magnetic oscillations in stations data during B_z southward magnetization. After more than 4 h of northward B_z that occurred around the storm onset (04:45 UT on 17 March), two main southward incursions of the B_z (about −25 nT) are noticed. During these two events, noticeable magnetic fluctuations in D_l^H are observed simultaneously in the three sectors. One remarkable observation is the different magnetization present in D_l^H in the Asian and the American sectors. As such oscillations are present in all the stations during southward B_z, they are possibly related to DP2 oscillations during PPEF. Taking into account the time difference between the Asian and American stations (about 12 h), this feature could give us some insight about the mechanism of PPEF during both nighttime and daytime. The interval before the storm from 2:00 to 8:00 UT on 16 March and after the storm from 14:00 to 16:00 UT on 18 March are two clear examples of different magnetizations during southward B_z.

Using a band-pass filter, diurnal periods were extracted with a bandwidth of 8 h centered at 24 h, that is, 24 h ± 4 h. The results are plotted in Figure 10 (top and bottom). They represent the diurnal filtered D_l^H (2) for the three different sectors. The diurnal period is associated to D_{dyn} and its detailed discussion is presented in the next section. Figure 10 (top) shows the temporal difference among the three sectors starting with the Asian and ending with the American one. The temporal delay observed has the same time difference as their

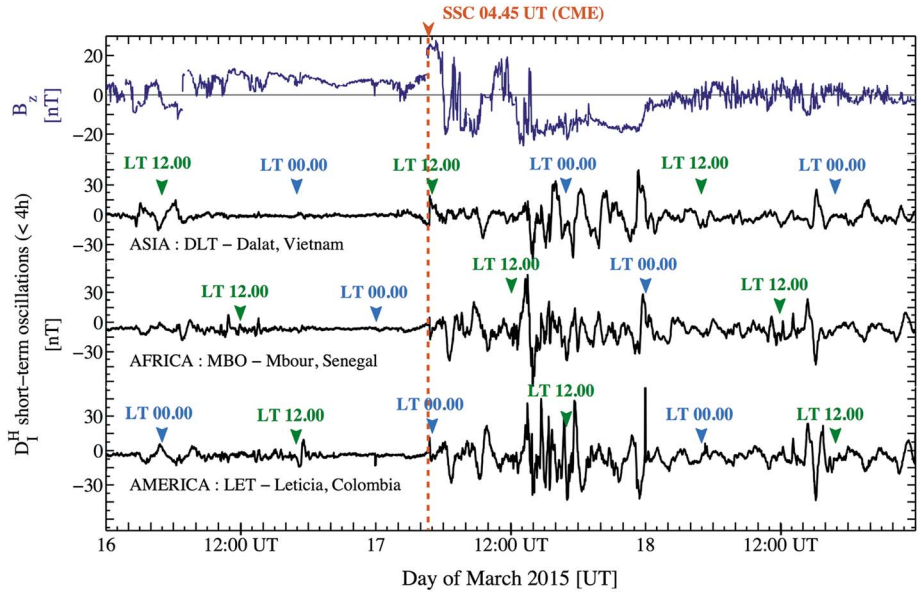

Figure 9. Magnetic disturbance of the *H* component due to PPEF at specific longitudinal sectors, from 16 to 18 March, from top to bottom are plotted the B_z component of IMF; the D_I^H short-term oscillations for the Asian, African, and American sectors.

respective local time. The most evident feature is the large increase during the main phase of the storm and its gradual decrease the days after. Regarding the presence of these diurnal periods, it is noticed that in the Asian sector the perturbation lasts longer (8 days), followed in time by the African (6 days) and American sectors (5 days), respectively. This feature is also observed in Figure 8.

We wrote in Table 2, column 6 the duration of the D_{dyn} in the different longitude sectors.

Figure 11 shows, from top to bottom, vTEC, f_oF_2, slab thickness τ, and h_mF_2 for the days before, during, and after the geomagnetic storm at two low-latitude locations in the Asian (first to fourth panels) and American sectors (fifth to eighth panels). On each panel the regular variation of the mentioned quantities is also indicated (blue curves). The reference daily variation for vTEC is determined from the average values of 12 to 15 March. As a reference for the daily variation of the other ionospheric parameters, 15 March 2015 has been selected being a quiet day with $Kp < 3^-$.

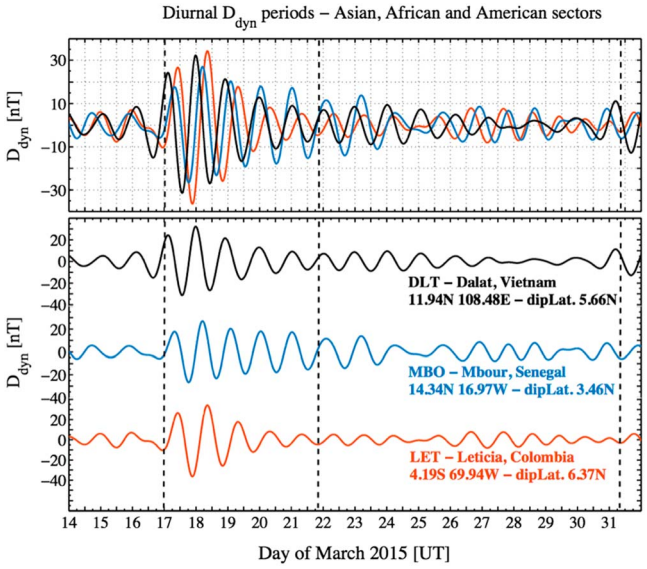

Figure 10. Magnetic disturbance D_{dyn} of the *H* component, at specific longitudinal sectors, from 14 to 31 March; (top) D_{dyn} in the three different sectors are plotted; (bottom) D_{dyn} disturbance in the Asian, African, and American sectors are plotted.

At fomo location (Asian sector, first to fourth panels) a significant vTEC decrease of about 70 total electron content unit (TECU) (1 TECU = 10^{16} m^{-2}) is observed during the day of 18 March. In the same period also f_oF_2 (as measured by Sanya ionosonde) exhibits a decrease if compared to its corresponding reference quiet day values. As far as h_mF_2 is concerned, the main feature observed from the reported data is a double peaked structure on 17 March, with maxima of ~450 km around 16:00 UT and 22:00 UT. In this location, the increase in the slab thickness during the local minimum of

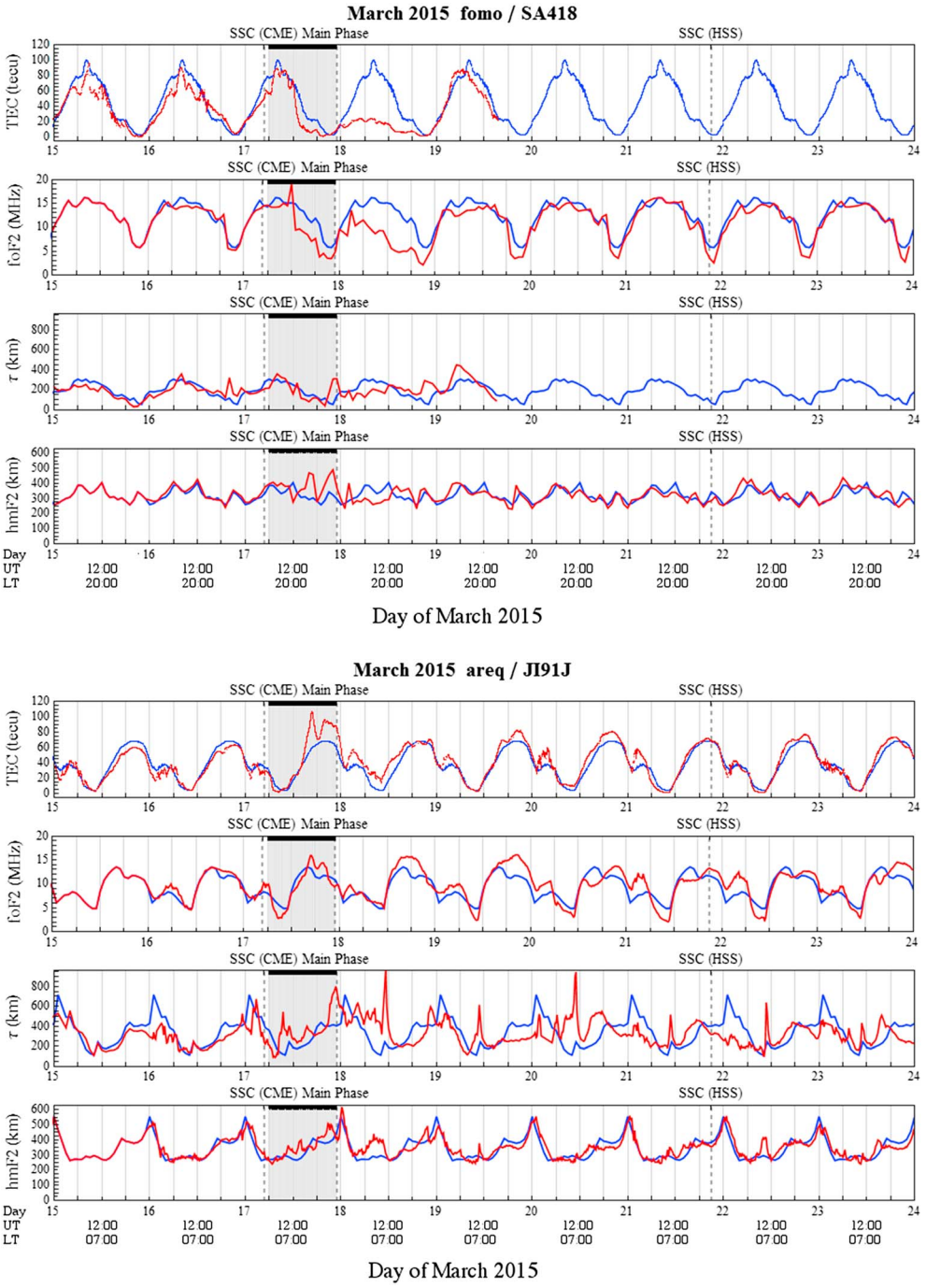

Figure 11. vTEC and F_2 layer peak parameters in the Asian and American sectors from 15 to 24 March; on each panel the regular (blue) and the disturbed (red) variations are superimposed. From top to bottom vTEC, f_oF_2, slab thickness, and h_mF_2 are shown.

vTEC at night on 17 March (and 18 March) is rather associated with the decrease of the f_oF_2 than to an increase in vTEC, which does not vary. Similar behavior of these ionospheric parameters is also observed at Wuhan location (data are not shown in the present paper).

At Arequipa location (areq, American sector, fifth to eighth panels), during the development of the main phase of the storm, a double peaked increase in vTEC of about 30 TECU is observed in the second half of 17 March. The f_oF_2 (as recorded by Jicamarca ionosonde) shows the same kind of response, with the

fluctuations appearing in the second part of the UT day. With reference to the height of the *F*2 layer peak density, no particular trends are observed on 17 March and only faster h_mF_2 variations than in the case of the quiet day are noticed. A moderate increase of the slab thickness is observed in predown hours on 17 March, while a more remarkable increase in τ is evident during 18 and 19 March. In these two days no particular trends in vTEC are present, while a positive storm effect is still observed in f_oF_2.

In both the Asian and American locations, the predawn increase in slab thickness can be seen and it is more remarkable in the station corresponding to American sector on 18 March. Nevertheless, due to the limited amount of ionosonde data available, an attempt to generalize the results in terms of slab thickness behavior could not be done.

Indeed, *Davies and Liu* [1991] reported that the pronounced predawn increase in slab thickness is caused by low values of N_mF_2, which in turn are probably connected with the decrease or reverse of the neutral wind [*Rishbeth*, 1989]. The increase in the slab thickness during the pre sunrise hours at low and middle latitudes has been reported by several authors [*Jayachandran et al.*, 2004, and references therein]. From these results, it is confirmed that slab thickness behavior is highly dependent on the geographic location of the observing site, as well as the diurnal, solar, and magnetic activity conditions.

4. Discussion

In section 3 we described in detail the observations. In this section, we will discuss point by point the results in order to interpret them. In Table 2, we have set up together the main characteristics of the storm depending on the longitudinal sector.

The storm began on 17 March when the CME hit the Earth. There is a very long compression phase (from 04:45 UT to 06:20 UT). Then the main phase of the storm started. In Figure 2, we see several periods of energy transfer as detected by the *AE* magnetic index (which is an indicator of the energy transferred from the solar wind to the magnetosphere). A first *AE* maximum (EI; 1016 nT) occurs around 09:00 UT; a second one (EII; 2298 nT) around 13:30 UT; after this second maximum the *AE* index remains large (EIII; $>$1000 nT) from ~16:30 UT to ~22:00 UT. On 17 March, the GEC exhibits two strong increases, one about 11:30 UT (several hours after EI) and one at 17:30 UT (several hours after EII) and a smaller increase later on at 00:00 UT on 18 March (see Figure 3). Columns 2 and 3 of Table 2 give the amplitude and time of occurrence of the maxima/minima of REC. The response to the first input (EI; $AE = 1016$ nT) is a positive storm effect in the Asian and African sectors, followed by a small negative storm effect only in the Asian sector. The response to the second input (EII $AE = 2298$ nT) is a positive storm effect in the African and American sectors. No remarkable effects have been detected as a consequence of EII in the Asian sector. At the time of EII, the Asian sector is on the evening side. The third peak in GEC is due to the positive storm in the American sector and is related to the input energy EIII ($AE > 1000$ nT, during several hours). Then, negative storm effects occur in all the longitudinal sectors starting from Pacific and Asia and followed by Africa and America as also observed by *Astafyeva et al.* [2015]. The largest negative storm effect is found in the Asian sector, and this is well explained through simulations by *Fuller-Rowell et al.* [1994]. *Fuller-Rowell et al.* [1994] have shown that the maximum response is observed in the sector that is on the night side when the storm starts. At the beginning of the storm at 04:45 UT, the Asian sector is on the dayside (~12:00 LT) and the perturbation during the main phase of the storm, on 17 March, is less remarkable in the Asian sector than in the African sector (that is on the morning side, ~ 04:45 LT, at the beginning of the storm) and the American sector (that is on the night side, ~ 00:00 LT, at the beginning of the storm) as inferred from vTEC maps in Figure 4. *Fuller-Rowell et al.*, [1994] have indicated that the least affected sector is the one on the dayside when the storm begins. We can see from Figure 4 that in the Asian sector the vTEC behavior is mostly regular, except on the day after the storm where a large TEC decrease (associated to the energy inputs EII and EIII occurring when the Asian sector is on the evening/night side) is observed.

The differences of response among the three sectors are clearly understood by theoretical approaches, but we have to consider the different storm energy inputs and not just the beginning of the storm. *Fuller-Rowell et al.*, [1994] explained as follows: "Joule heating at high latitudes raises the temperature of the upper atmosphere, and the heat sources drive a global wind surge from both polar regions which propagates to low latitudes, the global wind surge has preference for night sector and for the longitude of the magnetic pole and therefore depends on the UT start time of the storm." The simulations also indicate that the negative phases are primarily in response to the composition bulge and its movement

through the day. We clearly observed in Figure 5 the decrease of $[O/N_2]$ in the sectors where the negative storm effect is the largest, i.e., in the Asian sector and in the southern part of the American sector, so we can conclude that the theoretical model can partially explain the observations concerning the large negative phases.

In their numerical simulation *Fuller-Rowell et al.* [1994] did not include the electric field penetration to low latitudes neither the ionospheric disturbance dynamo. In our work, using magnetic data we tried to analyze the PPEF and DDEF, as these electric fields impact the variation of the Earth's magnetic field. In Figure 7, the part of the Earth's magnetic field generated by the disturbed ionospheric electric currents is plotted in red. On the days after the storm, at all longitudes a circulation of the disturbed ionospheric electric current opposite to the regular one S_R^H is inferred from its associated magnetic fluctuations D_l^H. Such result was found by *Blanc and Richmond* [1980]. We observe also short-time variations superimposed to the main diurnal variation. To interpret these results, we use the WPS. The results are shown in Figure 8.

In Figure 8, we easily recognize three kinds of perturbations based on their periodicity: (1) short-term oscillations, (2) diurnal and semidiurnal oscillations, and (3) planetary waves.

Using a high-pass filter, the periods lower than 4 h have been isolated and presented in Figure 9. Most of the short-term magnetic oscillations are observed during daytime throughout the main and recovery phases of the storm. Some of these short-time variations are related to the PPEF and its mapping from high latitudes to low latitudes, as they occur simultaneously at all the longitude sectors (see Figure 9). The DP2 equivalent current system and its variations are also characterized by quasi-periodic oscillations with time scales around half an hour to roughly 2 h. They are associated to the oscillations of B_z [*Nishida*, 1968; *Kikuchi et al.*, 1996]. However, it is expected to find a different magnetic response on H to PPEF in both nightside and dayside because of the different zonal direction of the mapped electric field, which is eastward in the dayside and westward in the night side. Despite the previous statement, it is not easy to detect DP2 fluctuations during nighttime as the electrical currents that respond to them are almost zero at night, due to very low conductivity. Nevertheless, it is possible to detect such fluctuations just if there is enough plasma in the *E* region to allow electric currents to flow, as it is the case when the nighttime sporadic *E* layer is present. A recent work by *Abdu et al.* [2013] shows how the westward polarization of the mapped electric field during PPEF at night could be the source of sporadic *E* layers. An evidence of this is shown in Figure 9, where fluctuations in the Asian sector around noon and midnight present different magnetization compared to those registered at the American sector at midnight and noon, respectively. To support this, during the days 16, 17, and 18 March, sporadic *E* layers during nighttime have been detected in the Asian sector by the Sanya ionosonde. We also notice that not all the D_l^H fluctuations are related to PPEF, as some of them are not simultaneous at all stations.

By using a band-pass filter, we isolated the diurnal component associated with the D_{dyn} in Figure 10. The D_{dyn} is the equivalent current system associated to DDEF [*Le Huy and Amory-Mazaudier*, 2008]. Some relevant features are noticed. The first one is the temporal difference among the three sectors that is expected because of their dependence with the diurnal behavior of the electric conductivity. This first characteristic does not give us any certainty about the temporal propagation of the thermospheric disturbance. The second feature is the temporal decay of the phenomena at each sector that is clearly shown in Figures 8 and 10. This is due to the fact that the D_{dyn} is just a response of the ionosphere to a large thermospheric disturbance, and it is determined by the *E* region lifetime. The D_{dyn} effect ends at different times depending on the considered sector (see Table 2, column 6). *Fathy et al.* [2014] analyzed the D_{dyn} disturbance related to CME and a HSSWS. They have found that the main component of D_{dyn} is a diurnal oscillation and have found also that the duration of the diurnal oscillation was different from one longitude sector to another. In Figure 8, a well-defined D_{dyn} diurnal oscillation during and after 17 March is found. For the same period, semidiurnal oscillations are also noticed with less strength than the diurnal ones. Some works have recently shown an apparent relationship of geomagnetic activity with diurnal and semidiurnal oscillations in the atmosphere. *Müller-Wodarg et al.* [2001] using a version of the Coupled Thermosphere-Ionosphere-Plasmasphere model suggest that at middle to high latitudes in situ diurnal and semidiurnal oscillations are produced by Joule heating and ion drag during active geomagnetic conditions. Observations reported in other studies [i.e., *Kunitake and Schlegel*, 1991; *Nozawa and Brekke*, 1995; *Fesen*, 1997] are in agreement with the theoretical results presented above.

5. Summary and Conclusion

In this paper, different kinds of data and analysis techniques have been contemporarily employed to investigate at a global scale the ionosphere response to the St Patrick's Day storm. Different features observed in the considered longitudinal sectors have also been characterized:

1. Positive storm effects are observed in the REC data: one increase in the Asian sector, two increases in the African and American sectors, and no increase in the Pacific sector.
2. The positive storm effects are related to different inputs of energy as indicated by the *AE* magnetic index.
3. The strongest positive storm effect in vTEC is observed in the American sector, which was on the nightside when the CME hit the Earth, on 17 March 2015. It is well described by the model of *Fuller-Rowell et al.* [1994], which shows that the strongest effect of a storm is detected at the location on the night side at the beginning of the storm.
4. A negative storm effect in the REC, vTEC, and in $[O/N_2]$ is observed in all the longitudinal sectors, mainly at middle and high latitudes.
5. In the Asian sector the negative storm effect starts earlier than in other longitude sectors, on 17 March and continue on 18 March. On 18 March, the vTEC maps show that most of the electron content is confined in the equatorial zone.
6. The impact of the negative phase is the largest in the Asian sector. This negative phase is related to very large inputs of energy (*AE* ~ 2300 nT and *AE* above ~1500 nT) occurring when the Asian sector is on the evening and night sides.
7. The vTEC maps show that the return to the normal level of ionization at middle and high latitudes occurs later in the Asian sector (~25 March) than in the African and American sectors (~23 March).
8. The analysis of the magnetic variations shows the presence of a diurnal component, which produced a reversed diurnal variation of the Earth's magnetic field, compared to the regular quiet one. This is the signature of the D_{dyn} equivalent current system, related to the disturbance dynamo;
9. By using the wavelet analysis of the magnetic field variations, at low latitudes, we extract a storm diurnal oscillation. This diurnal component lasts about 8 days in the Asian sector, about 6 days in the African sector, and about 5 days in the American sector;
10. By using the wavelet analysis of the magnetic field variation we extracted short-term oscillations (~2 h period). They are associated to oscillations of the southward B_z component of the IMF and occur simultaneously in all the longitudinal sectors during the storm period. These oscillations characterize the DP2 equivalent current system and are due to the PPEF;
11. We also noticed the existence of these short-term oscillations at nighttime, and we explained this fact by the presence of sporadic *E* layer at nighttime.

We interpret our results using the following theoretical works:

1. The coupled thermosphere-ionosphere model of *Fuller-Rowell et al.* [1994] that computes the changes in the motion and composition of the atmosphere and their impact on ionization, during magnetic storms.
2. The model of ionospheric disturbance dynamo proposed by *Blanc and Richmond* [1980] that estimates the dynamo effect of the storm thermospheric winds (due to auroral Joule heating) on the ionospheric electric fields and currents (DDEF and D_{dyn}).
3. The magnetospheric convection model of *Vasyliunas* [1970] that computes the effect of the penetration of the magnetospheric convection electric field from high to low latitudes (PPEF and DP2).

These theoretical works partially analyzed the response of the ionosphere to a storm, taking into account only one specific physical process for one single event. An attempt should be made to develop a numerical simulation for the St Patrick's Day storm, taking into account all the physical processes involved.

Acknowledgments
The authors are grateful to the IGS Community for making available GNSS data, the University of Massachusetts at Lowell-Center for Atmospheric Research for providing access to the digital ionogram database (DIDBase) and the GIRO data resources http://spase.info/SMWG/Observatory/GIRO, the Universitat Politecnica de Catalunya (UPC-IonSAT) for providing the VTEC data (UQRG IONEX files, in the framework of the MONITOR 2 ESA Project), Low Latitude Ionospheric Sensor Network (LISN), and Intermagnet Communities for providing the magnetic data used in this work.

References

Abdu, M. A., J. R. Souza, I. S. Batista, B. G. Fejer, and J. H. A. Sobral (2013), Sporadic *E* layer development and disruption at low latitudes by prompt penetration electric fields during magnetic storms, *J. Geophys. Res. Space Physics*, *118*, 2639–2647, doi:10.1002/jgra.50271.

Abdu, M. A., J. H. Sastri, J. MacDougall, I. S. Batista, and J. H. A. Sobral (1997), Equatorial disturbance dynamo electric field longitudinal structure and spread *F*: A case study from GUARA/EITS campaigns, *Geophys. Res. Lett.*, *24*, 1707–1710, doi:10.1029/97GL01465.

Abdu, M. A., J. H. Sastri, H. Lühr, H. Tachihara, T. Kitamura, N. B. Trivedi, and J. H. A. Sobral (1998), DP2 electric field fluctuations in the duskside dip equatorial ionosphere, *Geophys. Res. Lett.*, *25*, 1511–1514, doi:10.1029/98GL01096.

Abdu, M. A., T. K. Ramkumarb, I. S. Batistaa, C. G. M. Bruma, H. Takahashia, B. W. Reinischc, and J. H. A. Sobrala (2006), Planetary wave signatures in the equatorial atmosphere–ionosphere system, and mesosphere- *E*- and *F*-region coupling, *J. Atmos. Sol. Terr. Phys.*, *68*, 509–522.

Afraimovich, E. L., E. I. Astafyeva, and I. V. Zhivetiev (2006), Solar activity and global electron content, *Dokl. Earth Sci.*, *409A*(N6), 921–924.

Astafyeva, E., I. Zakharenkova, and M. Forster (2015), Ionospheric response to the 2015 St Patrick's day storm: A global multi-instrumental overview, *J. Geophys. Res. Space Physics*, *120*, 9023–9037, doi:10.1002/2015JA02629.

Blanc, M., and A. D. Richmond (1980), The Ionospheric disturbance dynamo, *J. Geophys. Res.*, *85*(A4), 1669–1686, doi:10.1029/JA085iA04p01669.

Chapman, S., and V. C. A. Ferraro (1931), New theory of magnetic storms, *Terr. Magn. Atmos. Electr.*, *36*, 77–97.

Chen, P. R. (1992), Two-day oscillations of the equatorial ionization anomaly, *J. Geophys. Res.*, *97*(A5), 6343–6357, doi:10.1029/91JA02445.

Cherniak, L., and I. Zakharenkova (2015), Dependence of the high-latitude plasma irregularities on the auroral activity indices: A case study of the 17 March 2015 geomagnetic storm, *Earth Planets Space*, *67*, 151, doi:10.1186/s40623-015-0316x.

Ciraolo, L., F. Azpilicueta, C. Brunini, A. Meza, and S. M. Radicella (2007), Calibration errors on experimental slant total electron content (TEC) determined with GPS, *J. Geod.*, *81*(2), 111–120.

Davies, K., and X. M. Liu (1991), Ionospheric slab thickness in middle and low latitudes, *Radio Sci.*, *26*(4), 997–1005, doi:10.1029/91RS00831.

Fathy, I., C. Amory-Mazaudier, A. Fathy, A. M. Mahrous, K. Yumoto, and E. Ghamry (2014), Ionospheric disturbance dynamo associated to a coronal hole: Case study of 5–10 April 2010, *J. Geophys. Res. SpacePhysics*, *119*, 4120–4133, doi:10.1002/2013JA019510.

Fejer, B. G., and L. Scherliess (1997), Empirical models of storm-time equatorial zonal electric fields, *J. Geophys. Res.*, *102*, 24,047–24,056, doi:10.1029/97JA02164.

Fejer, B. G., M. F. Larsen, and D. T. Farley (1983), Equatorial disturbance dynamo electric fields, *Geophys. Res. Lett.*, *10*, 537–540, doi:10.1029/GL010i007p00537.

Fesen, C. (1997), Geomagnetic activity effects on thermospheric tides: A compendium of theoretical predictions, *J. Atmos. Terr. Phys.*, *59*, 785–803.

Forbes, J. M., M. E. Hagan, S. Miyahara, F. Vial, A. H. Manson, C. E. Meek, and Y. Portnyagin (1995), Quasi-16-day oscillation in the mesosphere and lower thermosphere, *J. Geophys. Res.*, *100*, 9149–9161, doi:10.1029/94JD02157.

Forbes, J. M. (1996), Planetary waves in the thermosphere-ionosphere system, *J. Geomagn. Geoelec.*, *48*, 91–98.

Fuller-Rowell, T. J., M. V. Codrescu, R. J. Moffett, and S. Quegan (1994), Response of the thermosphere and ionosphere to geomagnetic storms, *J. Geophys. Res.*, *99*(A3), 3893–3914, doi:10.1029/93JA02015.

Gulyaeva, T. L., F. Arikan, M. Hernandez-Pajares, and I. Stanislawska (2013), GIM-TEC adaptive ionospheric weather assessment and forecast system, *J. Atmos. Sol. Terr. Phys.*, *102*, 329–340.

Gurubaran, S., S. Sridharan, T. K. Ramkumar, and R. Rajaram (2001), The mesospheric quasi 2-day wave over Tirunelveli, *J. Atmos. Terr. Phys.*, *63*, 975–985.

Harris, T. J. (1994), A long-term study of the quasi-two-day wave in the middle atmosphere, *J. Atmos. Terr. Phys.*, *56*, 569–579.

Hernandez-Pajares, M., J. M. Juan, and J. Sanz (1999), New approaches in global ionospheric determination using ground GPS data, *J. Atmos. Sol. Terr. Phys.*, *61*(16), 1237–1247.

Jayachandran, B., T. N. Krishnankutty, and T. L. Gulyaeva (2004), Climatology of ionospheric slab thickness, *Ann. Geophys.*, *22*, 25–33.

Jones, K. L. (1971), Storm time variation of the F_2 layer electron concentration, *J. Atmos. Terr. Phys.*, *33*, 379–389.

Jones, K. L., and H. Rishbeth (1971), The origin of storm increases of midlatitude *F*-layer electron concentration, *J. Atmos. Terr. Phys.*, *33*, 391–401.

Kikuchi, T., and T. Araki (1979), Horizontal transmission of the polar electric field to the equator, *J. Atmos. Terr. Phys.*, *41*, 927–936.

Kikuchi, T., H. Lühr, T. Kitamura, O. Saka, and K. Schlegel (1996), Direct penetration of the polar electric field to the equator during a DP2 event as detected by the auroral and equatorial magnetometer chains and the EISCAT radar, *J. Geophys. Res.*, *101*, 17,161–17,173, doi:10.1029/96JA01299.

Kobea, A. T., A. D. Richmond, B. A. Emery, C. Peymirat, H. Lühr, M. Moretto Hairston, and C. Armory-Mazaudier (2000), Electrodynamic coupling of high and low latitudes: Observations on May 27, 1993, *J. Geophys. Res.*, *105*, 22,979–22,989, doi:10.1029/2000JA000058.

Kunitake, M., and K. Schlegel (1991), Neutral winds in the lower thermosphere at high latitudes from 5 years of EISCAT data, *Ann. Geophys.*, *9*, 143–155.

Le Huy, M., and C. Amory-Mazaudier (2008), Planetary magnetic signature of the storm wind disturbance dynamo currents: D_{dyn}, *J. Geophys. Res.*, *113*, A02312, doi:10.1029/2007JA012686.

Le-Huy, M., and C. Amory-Mazaudier (2005), Magnetic signature of the ionospheric disturbance dynamo at equatorial latitudes, "D_{dyn}", *J. Geophys. Res.*, *10*, A10301, doi:10.1029/2004JA010578.

Mazaudier, C., and R. Bernard (1985), Saint-Santin radar observations of lower thermospheric storms, *J. Geophys. Res.*, *90*, 2885–2895, doi:10.1029/JA090iA03p02885.

Mazaudier, C., and S. V. Venkateswaran (1990), Delayed ionospheric effects of the geomagnetic storm of March 22, 1979 studied by the sixth coordinated data analysis workshop (CDAW-6), *Ann. Geophys.*, *8*, 511–518.

Mazaudier, C., R. Bernard, and S. V. Venkateswaran (1985), Correction to "Saint-Santin radar observations of lower thermospheric storms", *J. Geophys. Res.*, *90*, 6685–6686, doi:10.1029/JA090iA07p06685.

Müller-Wodarg, I. C. F., A. D. Aylwarda, and T. J. Fuller-Rowell (2001), Tidal oscillations in the thermosphere: A theoretical investigation of their sources, *J. Atmos. Sol. Terr. Phys.*, *63*, 899–914.

Nishida, A. (1968), Geomagnetic *DP* 2 fluctuations and associated magnetospheric phenomena, *J. Geophys. Res.*, *73*, 1795–1803, doi:10.1029/JA073i005p01795.

Nishida, A., N. Iwasaki, and N. T. Nagata (1966), The origin of fluctuations in the equatorial electrojet: A new type of geomagnetic variation, *Ann. Geophys.*, *22*, 478–484.

Nozawa, S., and A. Brekke (1995), Studies of the *E* region neutral wind in the disturbed auroral ionosphere, *J. Geophys. Res.*, *100*, 14,717–14,734, doi:10.1029/95JA00676.

Orus, R., M. Hernandez-Pajares, J. M. Juan, and J. Sanz (2005), Improvement of global ionospheric VTEC maps by using kriging interpolation technique, *J. Atmos. Sol. Terr. Phys.*, *67*(16), 1598–1609.

Pancheva, D., et al. (2004), Variability of the quasi-2-day wave observed in the MLT region during the PSMOS campaign of June–August 1999, *J. Atmos. Terr. Phys.*, *66*(6–9), 539–566.

Peymirat, C., A. D. Richmond, B. A. Emery, and R. G. Roble (1998), A magnetosphere–thermosphere–ionosphere electrodynamics general circulation model, *J. Geophys. Res.*, *103*, 17,467–17,477, doi:10.1029/98JA01235.

Rawer, K. (1963), *Meteorological and Astronomical Influences on Radio Wave Propagation*, pp. 221, Academy Press, New York.

Reinisch, B. W., and I. A. Galkin (2011), Global ionospheric radio observatory (GIRO), *Earth Planets Space*, *63*, 377–381, doi:10.5047/eps.2011.03.001.

Richmond, A. D., and R. G. Roble (1979), Dynamic effects of aurora generated gravity waves on the mid-latitude ionosphere, *J. Atmos. Terr. Phys.*, *41*, 841–852.

Rishbeth, H. (1989), Basic physics of the ionosphere, in *Radio-Wave Propagation*, edited by M. P. M. Hall and L. W. Barclay, pp. 75–94, Peter Peregrinus, London.

Sastri, J. H. (1988), Equatorial electric fields of ionospheric disturbance dynamo origin, *Ann. Geophys.*, *6*, 635–642.

Takahashi, H., R. A. Buriti, D. Gobbi, and P. P. Batista (2002), Equatorial planetary wave signatures observed in mesospheric airglow emissions, *J. Atmos. Terr. Phys.*, *64*, 1263–1272.

Testud, J., and G. Vasseur (1969), Ondes de gravité dans la thermosphère, *Ann. Geophys.*, *25*, 525–546.

Tulasi Ram, S., et al. (2016), Duskside enhancement of equatorial zonal electric field response to convection electric fields during the St. Patrick's Day storm on 17 March 2015, *J. Geophys. Res. Space Physics*, *121*, 538–548, doi:10.1002/2015JA021932.

Vasyliunas, V. M. (1970), Mathematical models of magnetospheric convection and its coupling to the ionosphere, in *Particles and Fields in the Magnetosphere*, edited by M. McCormac, pp. 60–71, Springer, New York.

Volland, H. (1979), Magnetospheric electric fields and currents and their influence on large scale thermospheric circulation and composition, *J. Atmos. Terr. Phys.*, *41*, 853–866.

Zhang, J. J., C. Wang, T. R. Sun, M. C. Liu, and K. Rwang (2015), GIC due to storm sudden commencement in low latitudes high-voltage power network in china observations and simulation, *Space Weather*, *13*, 643–655, doi:10.1002/2015SW001263.